Research Article

Zhixun Liang, Yunying Shi, Qiming Wu*, Yunfei Yi*, Yuanyuan Fan, and Peng Tang

An electro-optic half subtractor from a silicon-based hybrid surface plasmon polariton waveguide

https://doi.org/10.1515/phys-2024-0045
received February 28, 2024; accepted May 24, 2024

Abstract: In order to solve the problems of low transmission rate and large device size of electro-optical modulator, an electro-optic half subtractor based on silicon-based hybrid surface plasmon polariton waveguide is proposed in this study. The proposed device utilizes three units metal-oxide-semiconductor capacitor structure to achieve the half subtractor logic function of electro-optic control, improving the transmission rate of the electro-optic half subtractor while also reducing the device size using surface plasmon polariton technology, with a size of only 32 μm × 4.3 μm. At the same time, the use of hybrid silicon waveguides reduces the sharp Ohmic attenuation caused by surface plasmon polaritons and reduces optical insertion losses (ILs). The simulation results show that when the electro-optic half subtractor operates at the wavelength of 1,550 nm, the IL difference is 1.0 dB in each state, the transmission rate of the device is 0.75 Tbit/s, and the energy consumption is 12.69 fj/bit.

Keywords: electro-optic hybrid computing, half subtractor, hybrid surface plasmon polariton, ITO

*** Corresponding author: Qiming Wu,** School of Big Data and Computer, Hechi University, Yizhou, Guangxi, 541004, China, e-mail: 28032104@qq.com
*** Corresponding author: Yunfei Yi,** School of Big Data and Computer, Hechi University, Yizhou, Guangxi, 541004, China, e-mail: gxyiyf@163.com
Zhixun Liang: School of Big Data and Computer, Hechi University, Yizhou, Guangxi, 541004, China, e-mail: lzx478@163.com
Yunying Shi: School of Big Data and Computer, Hechi University, Yizhou, Guangxi, 541004, China, e-mail: 1404490856@qq.com
Yuanyuan Fan: School of Big Data and Computer, Hechi University, Yizhou, Guangxi, 541004, China, e-mail: 604335996@qq.com
Peng Tang: School of Big Data and Computer, Hechi University, Yizhou, Guangxi, 541004, China, e-mail: 1367426905@qq.com

1 Introduction

With the continuous development and widespread application of artificial intelligence technology in various fields, from deep learning to reinforcement learning, from computer vision to natural language processing, a large amount of computing resources and storage space are needed to support model training and data processing, including training and testing data [1–5]. These data need to be stored in the memory of high-performance computers for quick access and processing, in order to quickly update model parameters [6–11]. As a key component of the computing unit, the performance of optical logic devices directly affects the ability of optical logic operations. Products that have been widely used in optical communication are those that utilize the nonlinear effects of nonlinear media, such as semiconductor optical amplifiers, optical fibers, electric absorption modulators (EAMs), optical waveguide devices, photonic crystals, and other nonlinear media, to achieve all simple all optical logic operations. These products are technically mature, reliable, and easy to manufacture [12–15], but their drawback is that it is difficult to achieve silicon-based optoelectronic integration due to high power consumption and large volume. Kolli and Talabattula proposed a novel integrated optical serially coupled micro resonator based mechanical pressure sensor [16]. The device utilizes the method of heating the micro ring to achieve a specific wavelength of optical signal resonator, achieving the guidance of optical signals and realizing logical functions. Zhang *et al.* proposed an electro-optic half adder based on graphene and silicon-based hybrid integrated optical waveguides. This half adder exhibits excellent performance [17], with an extinction ratio greater than 41.05 dB, insertion loss (IL) less than 0.11 dB, and a data transmission rate of 10Gbit/s. Rezaei and Zarifkar proposed another electro-optic half adder and subtractor based on silicon-based hybrid integrated optical waveguides [18]. The device model structure was improved, and the performance was further improved. The sizes of the subtractor and adder were 0.31 and 0.64 μm^2,

respectively, thereby achieving miniaturization of the device. The logic device composed of micro ring resonators has poor thermal stability, low transmission rate, and large device volume due to the need to heat the device [19–23]. Although the electro-optic half adder based on a mixture of graphene and silicon-based materials has excellent performance and small device volume, the production process of graphene materials is complex and difficult to produce [23–25]. The all optical logic devices made using nonlinear effects, although achieve all optical logic operations, require higher pump light source signals to cause nonlinear phenomena in nonlinear media [26–33], resulting in high power consumption. Therefore, this study proposes an electro-optic half subtractor from a silicon-based hybrid surface plasmon polariton waveguide. The device size is compact, and each size in the model structure exceeds 10 nm, manufacturability. 3D-FDTD software is adopted for simulation, various size parameters in the device model were optimized, and the performance of each parameter of the device was finally solved. The detailed process of device principle, model design, and simulation verification are given further in this work.

2 The proposed model of half subtractor

The proposed model, as shown in Figure 1, has one optical input port and two output ports, Di and Bo, respectively. Silicon dioxide is the substrate, and silicon waveguides are etched on it. Three logic control units are set on top of the silicon waveguides. The optical signal is input from waveguide *c*, and two optical path control units are installed on waveguide *b*. The other end of waveguide *a* is connected to a Y-splitter, and one end of the Y-splitter is the Di output of the electro-optic half subtractor. One end of the Y-splitter and two waveguides form a logic control unit that controls the output of Bo. The optical signal is transmitted within the silicon waveguide, and the logic function of the electro-optic half subtractor is completed by applying voltage to control the three logic control units.

Table 1: Parameters of the device model

Parameter	Values (nm)
H_{ITO}	15
H_{SiO_2}	14
Gap	140
H_{AU}	500
Height of Si waveguide	340
Width of middle Si waveguide	275
Width of side Si waveguide	400

Referring to our previous research [21], the waveguide size and gap of the half subtractor, as well as the Indium–Tin–Oxide (ITO) film size settings in the control area, are shown in Table 1(a), with the H_{ITO}, H_{SiO_2}, gap, and H_{AU} values in the table are the thickness of ITO film, thickness of SiO_2 insulation layer, coupling distance between the waveguides, and thickness of the AU electrode, which are 15, 14, 140, and 500 nm, respectively. The height of the middle silicon waveguide and the sideways silicon waveguide are the same, but the width is different, which are 275 and 400 nm, respectively.

3 Methods

The Y-splitter and logic control unit have a high IL and extinction ratio on the entire half subtractor, so the logic

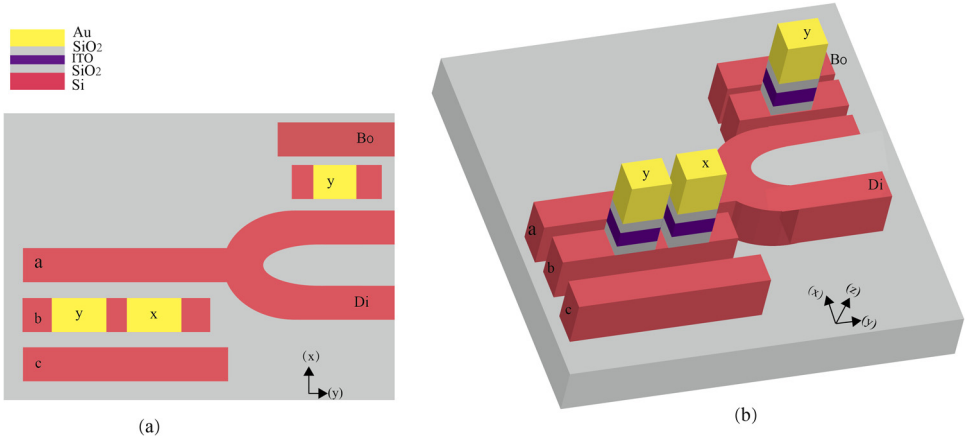

Figure 1: Model of the half subtractor: (a) top view of the half subtractor model and (b) 3D view of the half subtractor model.

control unit and Y-splitter are key components of the half subtractor. The theoretical minimum IL of a Y-splitter is 3 dB, but in reality, in a structure with a size of a few micrometers, the theoretical IL of a Y-splitter will exceed 3 dB. Therefore, the study of Y-splitters in the half subtractor needs to be focused on.

The half subtractor consists of three basic logic control units, which are composed of three waveguides, as shown in Figure 2. A control area is set on the middle waveguide, and metal-oxide-semiconductor (MOS) structure capacitance is achieved through ITO film sandwiched between SiO_2 insulation interlayer. The voltage is applied between the silicon waveguide and ITO thin film, and an appropriate voltage is applied to obtain the near zero state of the dielectric constant of the TCO material, thereby achieving EAM. Its dielectric constant conforms to the Drude model [26]:

$$\varepsilon = \varepsilon_\infty - \frac{N_{\mathrm{ITO}} q^2}{(\omega^2 + i\omega\gamma)\varepsilon_0 m^*}, \tag{1}$$

where the ε_∞ is the high frequency dielectric constant ($\varepsilon_\infty = 3.9$), N_{ITO} is the electron concentration of ITO materials, ω is the angular frequency, γ is the carrier scattering rate ($\gamma = 1.8 \times 10^{14}$ rad/s), m^* is the effective mass of charge carriers ($m^* = 0.35 m_0$, m_0 is the electronic quality, $m_0 = 9.31 \times 10^{-31}$ kg), q is an electronic charge ($q = 1.6 \times 10^{-19}$ C), and ε_0 is the free space dielectric constant ($\varepsilon_0 = 8.85 \times 10^{-12}$ F/m).

In order to calculate the variation in ITO carrier concentration by the voltage controlled, according to Kocakulah [27], this work used the following simple model for calculation:

$$N_{\mathrm{ITO}} = N_0 + \frac{\varepsilon_0 \cdot \kappa_{\mathrm{SiO_2}} \cdot V_g}{q \cdot H_{\mathrm{SiO_2}} \cdot H_{\mathrm{acc}}}. \tag{2}$$

According to Wang *et al.* [28], $N_0 = 1 \times 10^{19}$ cm^{-3} is the carrier concentration of ITO. $H_{\mathrm{SiO_2}}$ is the thickness of the insulating layer SiO_2 in the model structure, and the H_{acc} is the thickness of free charge carriers accumulated by SiO_2 below the ITO surface. According to the previous studies

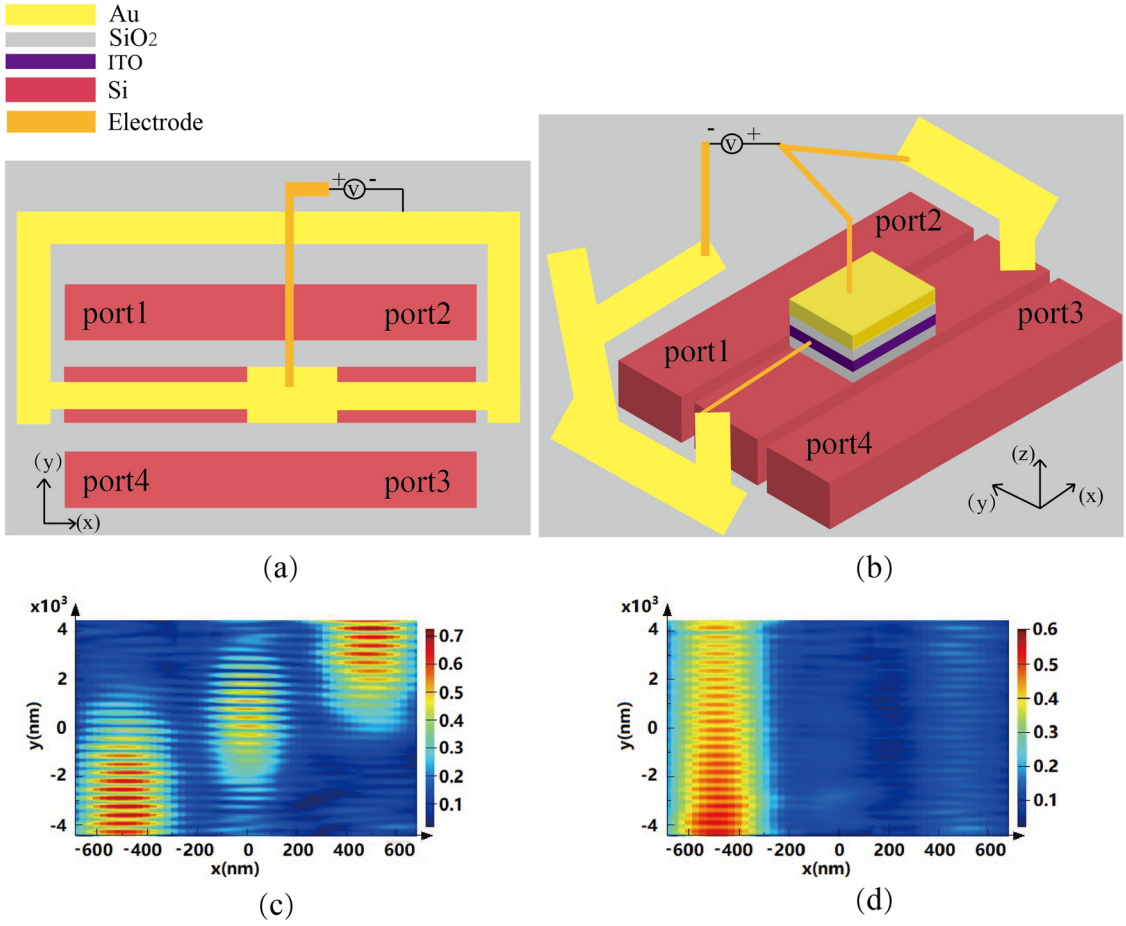

Figure 2: Logic control unit of the half subtractor. (a) Top view of logic control unit with added electrodes, (b) 3D view of logic control unit with electrodes, (c) electromagnetic field distribution of logic control unit without voltage applied, and (d) electromagnetic field distribution of logic control unit with voltage applied.

[27,28], H_{acc} = 7 nm, this thickness can also be obtained from the simulation study below. In this work, numerical device software was used to simulate and solve the variation in ITO carrier concentration under applied voltage. The applied voltage was from 0 to 4 V, with a step size of 0.01 V. The variation in carrier concentration is shown in Figure 3(d), while the variation in complex dielectric constant with voltage is shown in Figure 3(e). When the voltage is 2.35 V, the carrier concentration of the ITO activated material thin film is 6.57 × 10^{20} cm^{-3}, the real part of its composite dielectric constant is close to zero, the imaginary part is 0.671, and the corresponding refractive index is 0.54 + *i*0.43. When the voltage is 0 V, the carrier concentration of the ITO activated material thin film is 0.967 × 10^{19} cm^{-3}, the imaginary part of its composite dielectric constant is close to zero, the real part is 3.9, and the corresponding refractive index is 1.98 + *i*0.36. Next in FDTD software simulation, the refractive index of ITO material was simulated using the aforementioned refractive index.

The transmission rate is a key parameter indicator for measuring the performance of a half subtractor. The voltage control method in Figure 2(a) can be equivalent to the circuit shown in Figure 2(b), and finally can be simplified to the simplified circuit shown in Figure 2(c). According to Zhao *et al.* [26], the transmission rate of the half subtractor designed in this study can be calculated according to the MOS structure junction transmission rate, which is expressed by Eq. (3).

$$f_{max} = \frac{1}{2\pi RC}. \tag{3}$$

In the above equation, according to the definition of capacitor C, it can be represented as

$$C = \frac{\varepsilon_0 \varepsilon S}{d}, \tag{4}$$

where, ε_0 = 8.85 × 10^{-12} F/m, d is the thickness of SiO_2, S is the capacitance junction area, and $S = L_{coupling}\, W_{ig}$, based on previous research [34], the $L_{coupling}$ should be set to 8,900 nm, and W_{ig} is the waveguide width, ITO film width is consistent with waveguide width. R is the connection of the equivalent resistance of ITO. According to Zhao *et al.* [26], the equivalent resistance of silicon electrodes is assumed to be 500 Ω. In addition, the equivalent resistance of ITO activated material films can be expressed as

$$R_{ITO} = \frac{L}{\sigma S}, \tag{5}$$

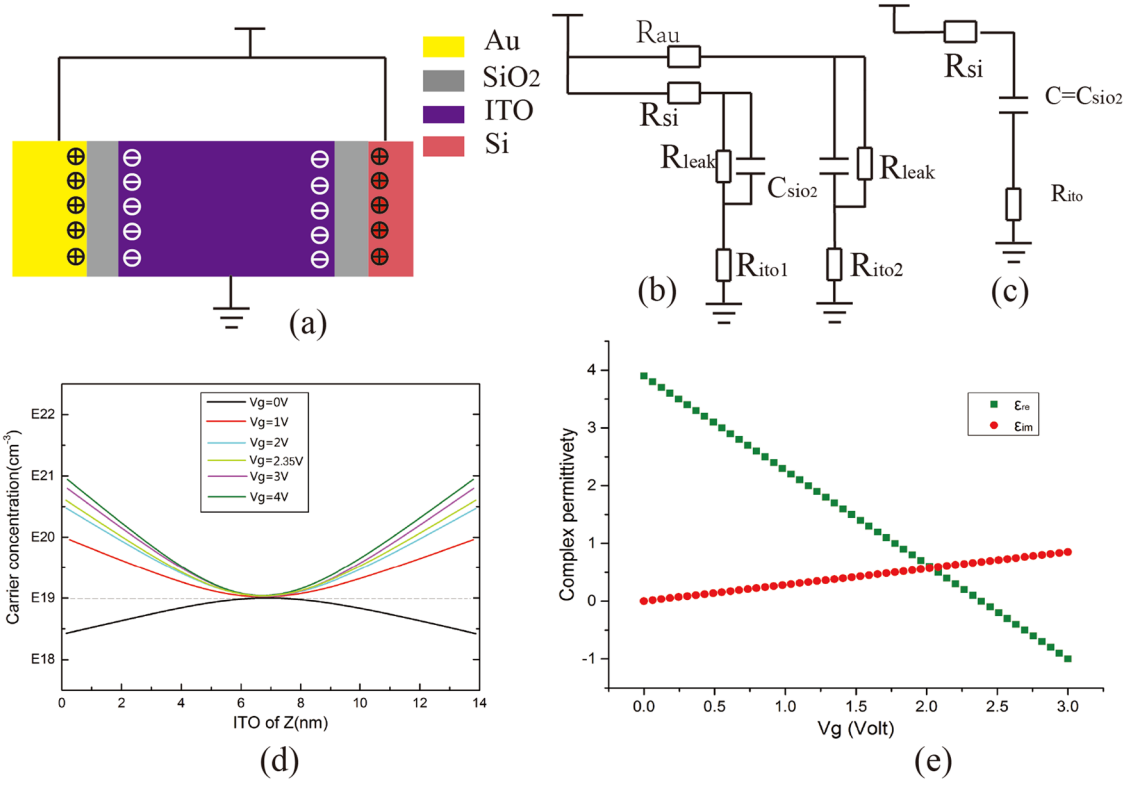

Figure 3: Characteristics of ITO film when applying voltage to the model. (a) Applied voltage model, (b) model equivalent circuit, (c) model equivalent circuit simplification, (d) changes in carrier concentration on applying voltage of 0–4 V, and (e) the composite dielectric constant of ITO varies with voltage.

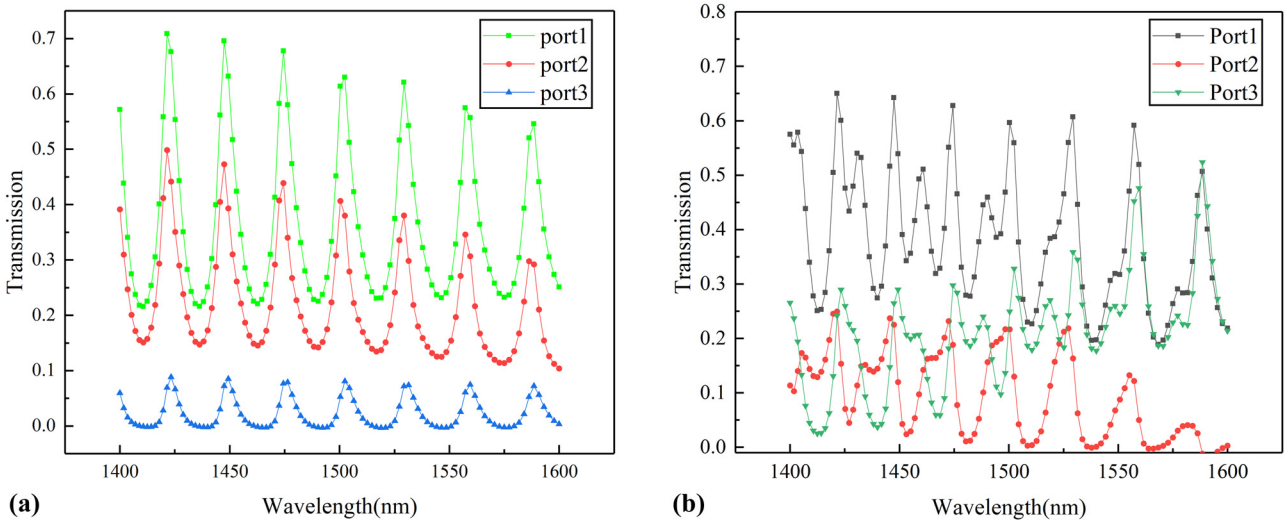

Figure 4: (a) Electromagnetic field intensity of ports 1–3 when the logic control unit operates in bar state and (b) electromagnetic field intensity of ports 1–3 when the logic control unit operates in the cross state.

where L is half of the thickness of the ITO film, $L = \frac{1}{2}H_{\mathrm{ITO}}$, S is the area of the device's ITO thin film, $S = L_{\mathrm{coupling}}\ W_g$, σ is the conductivity of ITO film, $\sigma = nq\mu_n$, as stated in the study by Alok and Sarang [29], carrier mobility of ITO thin film materials μ_n = 20 cm^2/V s, and n is the carrier concentration of ITO film. In this design, n is set as the carrier concentration when the voltage is 0 V, with a value of 0.967 × 10^{19} cm^{-3}, in fact, after applying a certain voltage to extrinsic semiconductor, the carrier concentration will be greater than the initial concentration [29]. Therefore, the equivalent resistance of the activated material thin film is actually smaller than the theoretical calculation value.

According to Zhao *et al.* [26], the power consumption required to transmit 1 bit can be calculated based on the charging energy of the capacitor (discharge does not require energy consumption), which can be expressed as

$$E = \frac{1}{2}CV^2, \tag{6}$$

where C is the capacity of the modulation region junction capacitance, and V is the operating voltage, and can be set at 2.35 V as stated by Alok and Sarang [29], Therefore, using Eqs. (1)–(6), the transmission rate of the device is calculated to be 0.75 Tbit/S, and the energy consumed is 12.69 fj/bit.

In addition, according to the definition of IL, the following equation can be used to represent the IL:

$$\mathrm{IL} = -10\log\frac{P_{\mathrm{out}}}{P_{\mathrm{in}}}, \tag{7}$$

where P_{out} is the intensity of the optical signal output from the waveguide by the device, and P_{in} is the intensity of the optical signal input to the waveguide by the device.

4 Simulation and analysis

FDTD software is used to simulate and study the logic control unit as shown in Figure 2. In Figure 2(a), the optical signal of TM mode is input from port 1. According to the electrodes of the logic control unit in Figure 2(b), under the condition of applying 2.35 V voltage or not applying voltage, the logic control unit operates in both bar and cross states, and the electromagnetic field strength of the optical signals of port 2 and port 3 is detected.

Figure 5 shows that the logic control unit operates in a bar state under applied voltage, and a TM mode wave with a wavelength of 1,400–1,600 nm and a gain of 1 is injected

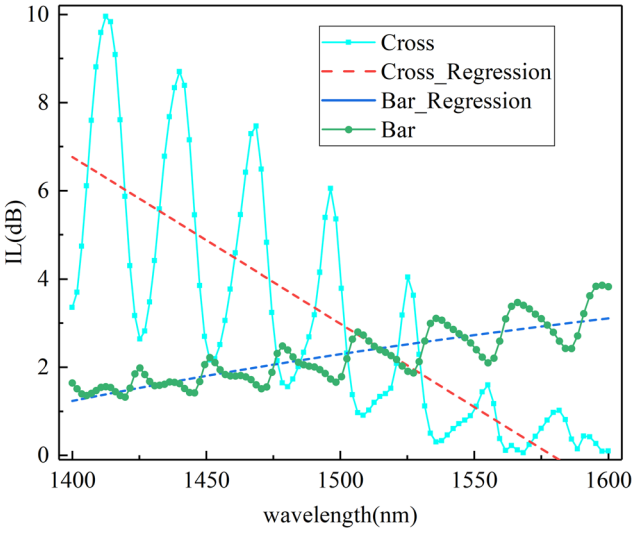

Figure 5: IL in cross and bar states.

from the port 1. The electromagnetic field strengths of port 2 and port 3 are observed from the transmittance in Figure 4. The average normalized electromagnetic field strength of port 1 is 0.36, and the average normalized electromagnetic field strength of port 2 is 0.22. The light transmittance is the best at the wavelength of 1,425 nm, exceeding 0.7. Due to the dispersion characteristics of optical materials, the transmittance varies periodically with wavelength. From the perspective of transmittance alone, at a wavelength of 1,550 nm, the average normalized electromagnetic field intensity of port 1 is 0.27, port 2 is 0.16, and port 3 is close to 0. Similarly, Figure 5 shows that the logic control unit operates in a cross state without applying voltage. A TM mode wave with a wavelength of 1,400–1,600 nm and a gain of 1 is injected from the port 1, and the optical signal electromagnetic field strengths of ports 2 and 3 are detected. At a wavelength of 1,550 nm, the average normalized electromagnetic field strength of port 1 is 0.59, the normalized electromagnetic field strength of port 2 is 0.05, and the normalized electromagnetic field strength of port 3 is 0.33.

The above is a study and analysis of the performance of a half subtractor from the perspective of transmittance. In order to further analyze the performance of a half subtractor, it is necessary to analyze the IL of optical devices. According to Eq. (7), the transmittance data of the cross and bar operating states can be calculated, and the ILs of the two states can be obtained separately. The results are plotted in Figure 5. From the figure, it can be seen that when the half subtractor operates in the cross state, the IL of the half subtractor decreases with the increase in wavelength. When the half subtractor operates in a bar state, the IL of the half subtractor increases with the increase in wavelength. Therefore, the IL of the device needs to balance the IL of the two states, and the average value can be taken to obtain the optimal IL. When the operating wavelength is about 1,580 nm, the minimum average IL is 1.3 dB. When the working wavelength is the common optical communication wavelength of 1,550 nm, the average IL is 1.7 dB. Among them, when the half attenuator operates in the cross and bar states, the IL is 1.0 and 2.3 dB, respectively.

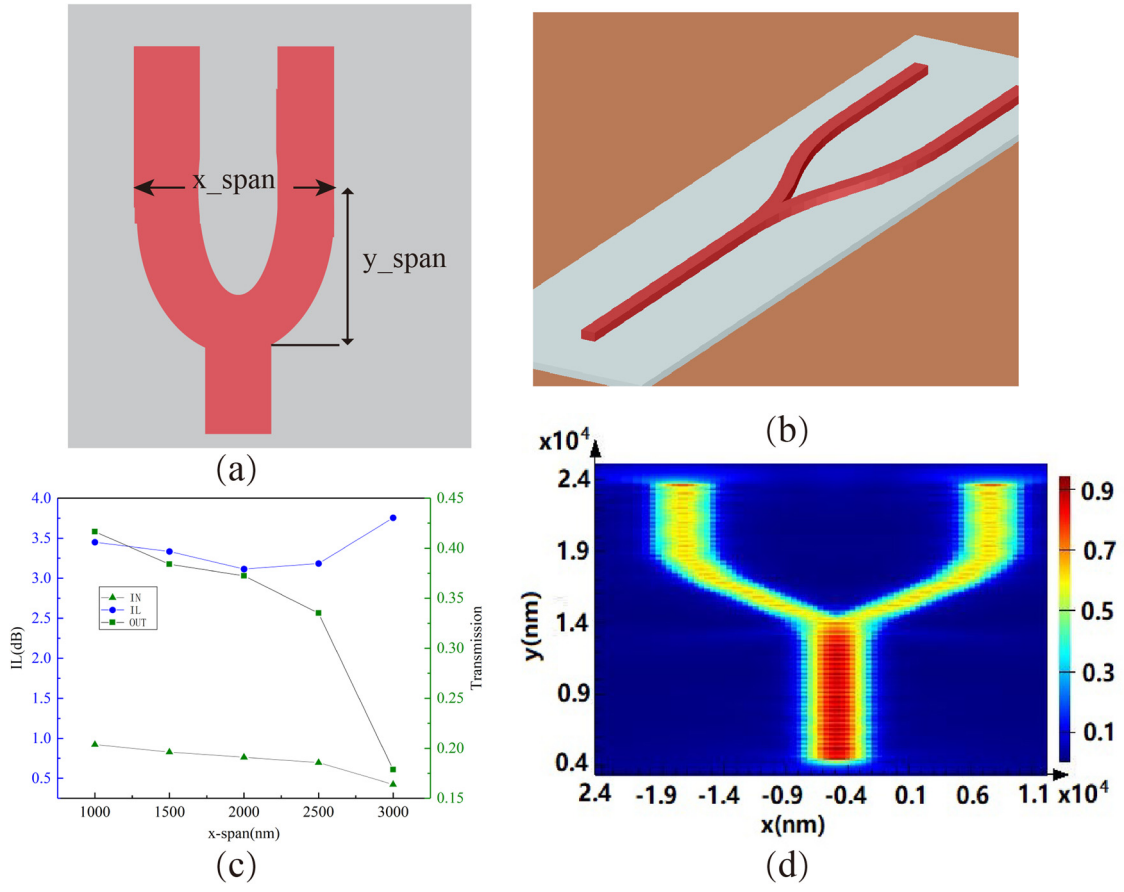

Figure 6: Performance analysis of Y-splitter with half subtractor. (a) Top view of Y-splitter, (b) 3D diagram of Y-splitter, (c) performance analysis of IL with *x*-span variation, and (d) electromagnetic field distribution diagram of Y-splitter in working state.

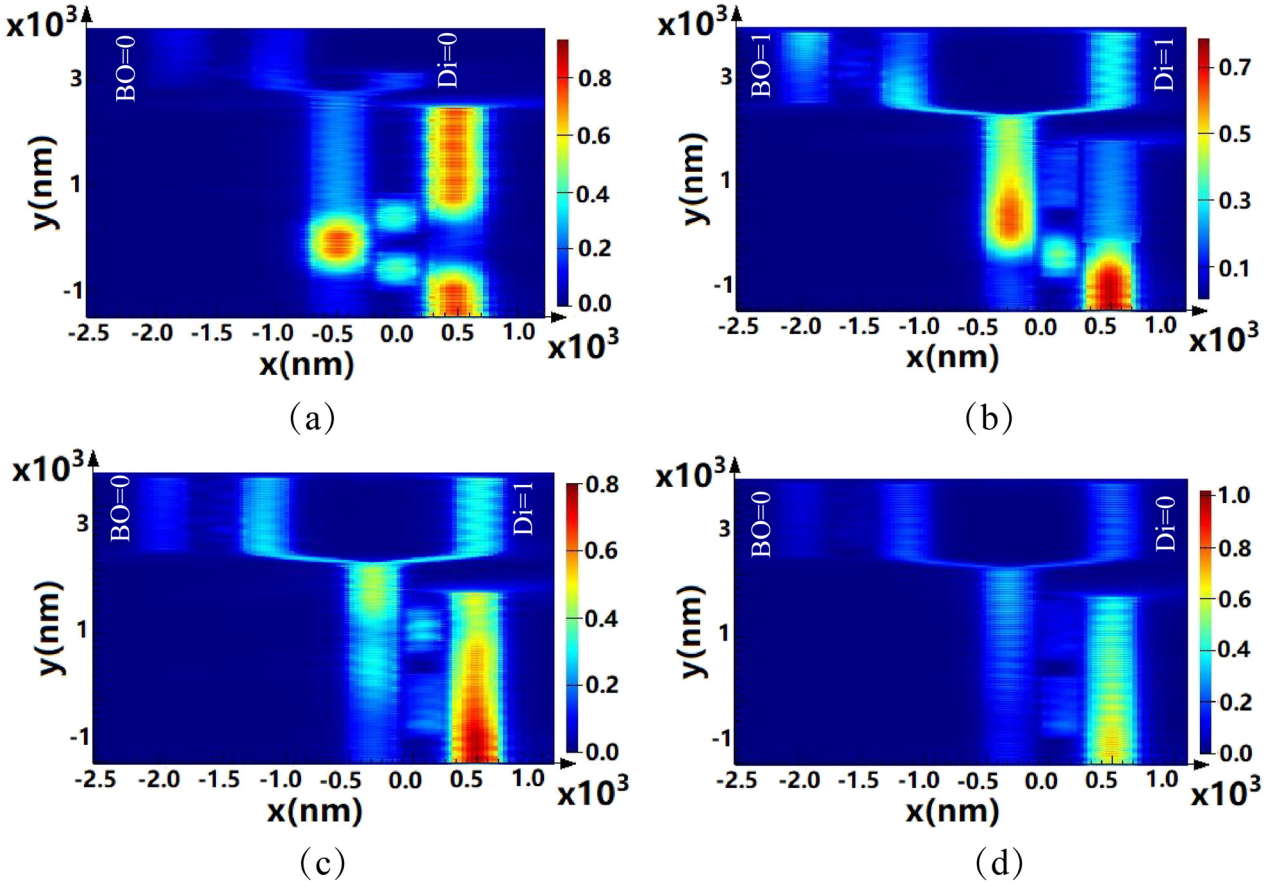

Figure 7: Electromagnetic field distribution during the operation of the half subtractor. (a)–(d) The electromagnetic field distribution of the half subtractor operating at 00, 01, 10, and 11 state, respectively.

In order to match the size of the entire device, we kept the silicon waveguide size of the Y-splitter consistent with the silicon waveguide size next to the logic control unit. At the same time, we fixed the *y*-span size of the Y-splitter to 4,000 nm, and the *x*-span size varied from 1,000 to 3,000 nm. We simulated the optical performance of the Y-splitter, and the results are plotted in Figure 6. From Figure 6(c), it can be seen that the *x*-span size should not be set too large or too small, and the curvature of the bent waveguide should be set within a reasonable range to minimize IL. From Figure 6(c), it can be seen that when the *y*-span size of the Y-splitter is fixed at 4,000 nm, it is advisable to set the *x*-span size to around 2,000 nm, and the IL of the Y-splitter is 3.11 dB.

FDTD software was used to simulate the entire half subtractor. The voltages were applied to the logic control unit in four states: 00, 01, 10, and 11. The detector was used to observe the distribution of electromagnetic fields in the *Z* direction. The simulation experiment results are shown in Figure 7. Figure 7(a)–(d), respectively, show the corresponding voltages applied to the logic control unit in four states: 00, 01, 10, and 11, The output ports of the half reducer BO and Di obtained four results: 00, 11, 01, and 00, respectively, verifying the correct logic of the half subtractor.

The above studies were conducted on a single logic control unit and a Y-splitter, respectively, to obtain the IL during the operation of the logic control unit and Y-type splitter. By calculation, when the half attenuator operates at a wavelength of 1,550 nm, the IL of BO and Di at the output port of the half device are 7.41 and 6.41 dB, respectively, when it operates at 01 state. When it operates at 10 state, the IL of Di at the output port is 6.41 dB, and the difference in IL is 1.0 dB.

5 Conclusion

In this study, based on the hybrid waveguide surface plasmon polariton technology, we Proposed an electro-optic hybrid half attenuator, with a size of only 32 μm × 4.3 μm, featuring ultra-compact dimensions. After we modeling, calculation, and analysis, we find that the transmission rate of the device is high. By modeling and analyzing

the logic control unit and Y-splitter, the principles for optical IL and Y-splitter size setting were obtained. The optical IL of the device differs by 1.0 dB, but the overall IL of the device is still relatively large, which is a problem that we need to solve in our future research work.

Acknowledgments: This work was supported by the Guangxi Natural Science Foundation Joint Funding Project (2021GXNSFBA220023), and in part by Hechi University high-level talents research project (No. 2022GCC010) and Research Basic Ability Improvement Project for Young and Middle-aged Teachers of Guangxi Universities (2023KY0633).

Funding information: This work was supported by the Guangxi Natural Science Foundation Joint Funding Project 2021GXNSFBA220023, in part by Key scientific research projects of Hechi University in 2021 (No. 2021XJZD001), and in part by Hechi University high-level talents research project (No. 2022GCC010) and Research Basic Ability Improvement Project for Young and Middle-aged Teachers of Guangxi Universities (2023KY0633).

Author contributions: All authors have accepted responsibility for the entire content of this manuscript and approved its submission.

Conflict of interest: The authors state no conflict of interest.

Data availability statement: All data generated or analyzed during this study are included in this published article.

References

[1] Rehioui H, Cuissart B, Ouali A, Lepailleur A, Lamotte JL, Bureau R, et al. New pharmacophore fingerprints and weight-matrix learning for virtual screening application to Bcr-Abl data. Mol Inform. 2023;42(1):e2200210.

[2] Long X, Gong X, Zhang B, Zhou H. Deep learning based data prefetching in CPU-GPU unified virtual memory. J Parallel Distrib Comput. 2023;174:19–31.

[3] Liu X, Song P. Virtual label guided multi-view non-negative matrix factorization for data clustering. Digit Signal Process. 2023;133:103888.

[4] Wei W, Zhang T, Yang J, Qian Y, Dong Y. Global virtual data space for unified data access across supercomputing centers. IEEE Trans Cloud Comput. 2023;11:1822–39.

[5] Wang N, Zhou R, Han L, Chen H, Li Z. Online scheduling of distributed machine learning jobs for incentivizing sharing in multi-tenant systems. IEEE Trans Comput. 2022;72(3):653–7.

[6] Aghapour Z, Sharifian S, Taheri H. Task offloading and resource allocation algorithm based on deep reinforcement learning for distributed AI execution tasks in IoT edge computing environments. Comput Netw. 2023;223:109577.

[7] Talib MA, Majzoub S, Nasir Q, Jamal D. A systematic literature review on hardware implementation of artificial intelligence algorithms. J Supercomput. 2021;77:1897–938.

[8] Fernández Pérez I, Prieta FD, Rodríguez-González S, Corchado JM, Prieto J. Quantum AI: Achievements and challenges in the interplay of quantum computing and artificial intelligence. International Symposium on Ambient Intelligence; 2023.

[9] Khanal B, Orduz J, Rivas P, Baker E. Supercomputing leverages quantum machine learning and Grover's algorithm. J Supercomput. 2023;79:6918–40.

[10] Kang JB, Shen AZ, Gurajala S, Nathan A, Rumker L, Aguiar V, et al. Integrated artificial intelligence and predictive maintenance of electric vehicle components with optical and quantum enhancements. Opt Quantum Electron. 2023;55(10):855–2268.

[11] Wang L, Wang Y, Qian M, Dong Y. Logical model design and controllability verification based on graphene oxide and metal ions. J Electron Inf Technol. 2020;42(6):1410–9.

[12] Cheng J, Jiang X, Zhou H, DongJian JI. Advances and challenges of optoelectronic intelligent computing. Chin J Lasers. 2022;49(12):1219001–13.

[13] Granpayeh A, Habibiyan H, Parvin P. Photonic crystal directional coupler for all-optical switching, tunable multi/demultiplexing and beam splitting applications. J Mod Opt. 2019;66(4):359–66.

[14] Janani K, Rajesh A, Shankar T. Design of an optical half-adder using cohesive twin-structured PCRR. J Comput Electron. 2018;17(2):837–44.

[15] Xu W, Li Y, Cui Q, Zhang H, Xia C, Guo H, et al. All-optical generation, detection, and manipulation of picosecond acoustic pulses in 2D semiconductor/dielectric heterostructures. Photonics Res. 2023;11(12):2000.

[16] Kolli VR, Talabattula S. An optimized integrated optical coupled micro ring resonator for low pressure sensing. IEEE Sens J. 2022;22:16016–26.

[17] Zhang J, Li S.-Q., Ding J, Wang P.-J, Chen WW. Design of an electro-optical half-adder based on silicon-graphene waveguides. J Optoelectron·Laser. 2018;29(8):805–10 (in Chinese).

[18] Rezaei MH, Zarifkar A. Subwavelength electro-optical half-subtractor and half-adder based on graphene plasmonic waveguides. Plasmonics. 2019;14(6):1939–47.

[19] Dong G, Wang Y, Zhang X. High-contrast and low-power all-optical switch using Fano resonance based on a silicon nanobeam cavity. Opt Lett. 2018;43(24):5977–80.

[20] Sun S, Narayana VK, Sarpkaya I, Crandall J, Soref RA, Dalir H, et al. Hybrid photonic-plasmonic nonblocking broadband 5 × 5 router for optical networks. IEEE Photonics J. 2017;10(2):1–12.

[21] Zhixun L, Yunying S, Yunfei Y, Yuanyuan F, Lvqing B. Electro-optic hybrid logic gate derived from a silicon-based hybrid surface plasmon polariton waveguide. J Nanoelectron Optoelectron. 2022;17:298–304.

[22] Yahya MR, Wu N, Yan G, Ge F, Ahmed T. RoR: A low insertion loss design of rearrangeable hybrid photonic-plasmonic 6 × 6 non-blocking router for ONoCs. IEICE Electron Express. 2019;16:20190346.

[23] Bai Y, Yu M, Lu L, Zhang D, Zhu L. Quantized photonic neural network modeling method based on micro ring modulators. Opt Eng. 2022;61(6):061409.

[24] Mahmud MT, Zhai D, Sandler N. Topological flat bands in strained graphene: substrate engineering and optical control. Nano Lett. 2023;23(16):7725–32.

[25] Tannaz S, Moradkhani M, Taherzade M, Rezaei MH. Ultracompact, high-extinction ratio XOR, OR, and Feynman logic gates based on plasmonic metal-insulator-metal directional couplers. Appl Opt. 2023;62:644–53.
[26] Zhao Y, Xing G, Zhao Y, Yu C, Liu Q, Zhao C, et al. Graphene aerogel modified with a vanadium nitride film by a sputtering method for use in high-performance supercapacitors. Mater Lett. 2020;261:127085.
[27] Kocakulah G. Comparison of electro-optical and dielectric properties of cobalt(II) phthalocyanine doped cholesteric liquid crystals. Opt Mater. 2023;141:113949.
[28] Wang L, Dong Y, Gao S, Chen KY, Fang FC, Jin GY. Research progress of perovskite materials in the field of lasers. China Opt. 2019;12(5):993–1014.
[29] Alok K, Sarang M. All optical NOR and NAND gates using four circular cavities created in 2D nonlinear photonic crystal. Opt Laser Technol. 2020;123:105910.
[30] Chen X, Li Z, Zhao R, He Y, He Y, Liang Z, et al. Flexible one-dimensional photonic crystal films composed of chalcogenide glass and water-soluble polymer for curvature sensing. Chin Opt Lett. 2024;22(1):021601.
[31] Abouelmagd EI, Awad ME, Elzayat EMA, Abbas IA. Reduction the secular solution to periodic solution in the generalized restricted three-body problem. Astrophys Space Sci. 2014;350(2):495–505.
[32] Abbas I, Saeed T, Alhothuali M. Hyperbolic two-temperature photothermal interaction in a semiconductor medium with a cylindrical cavity. Silicon. 2021;13(6):1871–8.
[33] Du B, Lu S, Liu Y. Periodic Solution for neutral-type neural networks in critical case. Neural Process Lett. 2016;44(3):765–77.
[34] Zhixun L, Yunying S, Yunfei Y, Yuanyuan F, Lvqing B. Electro-optic hybrid logic gate derived from a silicon-based hybrid surface plasmon polariton waveguide. J Nanoelectron Optoelectron. 2022;17(2):298–304.